You might find this additional information useful...

Supplemental material for this article can be found at:
http://jn.physiology.org/cgi/content/full/00470.2004/DC1

This article cites 40 articles, 20 of which you can access free at:
http://jn.physiology.org/cgi/content/full/92/5/2659#BIBL

This article has been cited by 2 other HighWire hosted articles:

Physiological Classification of Sympathetic Neurons in the Rat Superior Cervical Ganglion

C. Li and J. P. Horn
J Neurophysiol, January 1, 2006; 95 (1): 187-195.
[Abstract] [Full Text] [PDF]

Post-stimulus potentiation of transmission in pelvic ganglia enhances sympathetic dilatation of guinea-pig uterine artery in vitro
J. L Morris, I. L Gibbins and P. Jobling
J. Physiol., July 1, 2005; 566 (1): 189-203.
[Abstract] [Full Text] [PDF]

Updated information and services including high-resolution figures, can be found at:
http://jn.physiology.org/cgi/content/full/92/5/2659

Additional material and information about *Journal of Neurophysiology* can be found at:
http://www.the-aps.org/publications/jn

This information is current as of January 5, 2006 .

Estimating Use-Dependent Synaptic Gain in Autonomic Ganglia by Computational Simulation and Dynamic-Clamp Analysis

Diek W. Wheeler, Paul H. M. Kullmann, and John P. Horn
Department of Neurobiology and Center for the Neural Basis of Cognition, University of Pittsburgh School of Medicine,
Pittsburgh, Pennsylvania 15261

Wheeler, Diek W., Paul H. M. Kullmann, and John P. Horn.
Estimating use-dependent synaptic gain in autonomic ganglia by
computational simulation and dynamic-clamp analysis. *J Neurophysiol* 92: 2659–2671, 2004. First published June 22, 2004; 10.1152/
jn.00470.2004. Biological gain mechanisms regulate the sensitivity
and dynamics of signaling pathways at the systemic, cellular, and
molecular levels. In the sympathetic nervous system, gain in sensory-
motor feedback loops is essential for homeostatic regulation of blood
pressure and body temperature. This study shows how synaptic
convergence and plasticity can interact to generate synaptic gain in
autonomic ganglia and thereby enhance homeostatic control. Using a
conductance-based computational model of an idealized sympathetic
neuron, we simulated the postganglionic response to noisy patterns of
presynaptic activity and found that a threefold amplification in
postsynaptic spike output can arise in ganglia, depending on the
number and strength of nicotinic synapses, the presynaptic firing rate,
the extent of presynaptic facilitation, and the expression of muscarinic
and peptidergic excitation. The simulations also showed that postsyn-
aptic refractory periods serve to limit synaptic gain and alter postsyn-
aptic spike timing. Synaptic gain was measured by stimulating disso-
ciated bullfrog sympathetic neurons with 1–10 virtual synapses using
a dynamic clamp. As in simulations, the threshold synaptic conduc-
tance for nicotinic excitation of firing was typically 10–15 nS, and
synaptic gain increased with higher levels of nicotinic convergence.
Unlike the model, gain in neurons sometimes declined during stimu-
lation. This postsynaptic effect was partially blocked by 10 μM Cd^{2+},
which inhibits voltage-dependent calcium currents. These results
support a general model in which the circuit variations observed in
parasympathetic and sympathetic ganglia, as well as other neural
relays, can enable functional subsets of neurons to behave either as 1:1
relays, variable amplifiers, or switches.

INTRODUCTION

The synaptic organization of sympathetic and parasympa-
thetic ganglia enables spinal preganglionic neurons to control
autonomic behavior by driving postganglionic neurons. The
resulting transformation of motor activity depends on the
intrinsic ganglionic circuitry, whose anatomy incorporates pre-
synaptic divergence and postsynaptic convergence, while also
allowing for different forms of short-term plasticity and for
interplay between the ionotropic and metabotropic actions of
acetylcholine and peptidergic co-transmitters (Akasu and Nish-
imura 1995; Gibbins et al. 2000; Kuba and Koketsu 1978;
Simmons 1985; Smith 1994). Functional descriptions of auto-
nomic ganglia often stress their role as simple relays in which
divergence helps to provide peripheral targets with an adequate

level of neurally mediated excitation or inhibition (Iversen et
al. 2000; Jänig 1995; McLachlan 2003; Powley 2003). In
contrast, the consequences of convergence, plasticity, and
metabotropic modulation remain relatively unclear. To resolve
this issue, we have sought to develop a general method for
exploring ganglionic integration by combining theory and
simulations with cell physiology. Such an approach may illu-
minate the variations in function that have arisen through
phenotypic specialization in subsets of autonomic neurons and
through the evolutionary adaptations observed in ganglia from
different vertebrate species (Gibbins 1995; Gibbins et al. 2000;
Purves et al. 1986).

To develop a generic view of ganglionic organization, we
began by considering paravertebral sympathetic ganglia 9 and
10 of the bullfrog. This model system has many features that
facilitate experimental study (Smith 1994). These advantages
include *1*) low levels of synaptic convergence that can be
readily assessed, *2*) functional criteria that permit the physio-
logical identification and independent analysis of B and C
neurons, which selectively innervate cutaneous glands and
blood vessels, *3*) well-defined modulatory mechanisms of mus-
carinic and peptidergic co-transmission, and *4*) established
methods that permit the study of fully differentiated neurons
from dissociated ganglia in adult animals. In B-type neurons,
Karila and Horn (2000) have identified an $n + 1$ convergence
pattern of weak and strong nicotinic synapses, where every
postganglionic neuron receives one very strong, always su-
prathreshold, synapse and a variable number (*n*) of weak
synapses. Arguing that a similar pattern occurs in the paraver-
tebral ganglia of all vertebrates, they derived a mathematical
theory of ganglionic integration based on the principle of
stochastic coincidence detection. This approach led to the
broad prediction that, paravertebral sympathetic ganglia, in
general, behave as use-dependent synaptic amplifiers of
preganglionic activity. In this scheme, gain is regulated by the
number of converging nicotinic synapses and by their strength
and plasticity.

Although the coincidence detection theory of Karila and
Horn (2000) provided a simple means for understanding how
seemingly unrelated features of ganglionic organization could
interact to produce amplification, it was limited by a lack of
biophysical details describing ionic conductances and determi-
nants of synaptic plasticity. Schobesberger et al. (1999, 2000)
partially addressed this problem by adapting an earlier conduc-
tance-based model of the sympathetic B-type neuron (Yamada

et al. 1989) and examining the interaction between slow metabotropic excitation and subthreshold nicotinic excitatory postsynaptic potentials (EPSPs). The resulting analysis showed that muscarinic and peptidergic slow EPSPs could act to strengthen nicotinic synapses, but did not directly test the consequences for synaptic gain.

This study examines ganglionic integration by combining simulations of ganglionic activity with dynamic-clamp experiments. The simulations reveal how different patterns of preganglionic activity, in conjunction with synaptic mechanisms, control synaptic gain. In addition to clarifying certain limitations of the more minimal coincidence detection theory (Karila and Horn 2000), the present simulations establish the range of synaptic transformations of activity that may be implemented by different populations of autonomic neurons. In whole cell recordings from dissociated sympathetic B neurons, the dynamic-clamp method has been used to drive postsynaptic firing with different patterns of virtual synaptic activity. By taking this approach, one has precise control over the number, strength, and occurrence of each synaptic event and can compare the response of different cells to identical stimulation, an experimental procedure that would not be possible with living synapses. The experimental results confirm key predictions of the simulations and identify a postsynaptic role for calcium in regulating synaptic gain.

METHODS

Theoretical basis for simulations

The part of the autonomic system we are studying—sympathetic and parasympathetic ganglia—consists of a population of spinal, preganglionic presynaptic neurons connected via a simple network of synapses to a population of purely postsynaptic ganglionic neurons. As in previous work (Karila and Horn 2000), synaptic gain (G) has been defined as the multiplicative factor that relates the system's spike output to its input, where each is represented by their average firing rates (f_{pre}, f_{post}). Gain in this system has a simple physical interpretation. When $G > 1$, the postsynaptic neurons, on average, are firing faster than the presynaptic neurons

$$f_{post} = Gf_{pre} \qquad (1)$$

The multiplicative definition of gain (*Eq. 1*) is standard in control theory and has application to many problems including autonomic control of blood pressure (Khoo 2000). We refer to ganglionic gain as synaptic gain because it arises through synapses.

To simplify the task of simulating ganglionic integration, three central postulates were adopted from earlier work (Karila and Horn 2000). Each postulate represents an idealization of experimental observations.

POSTULATE 1—VARIATIONS IN CONVERGENCE FOLLOW AN $N + 1$ RULE IN SYMPATHETIC GANGLIA. Under this rule, every postganglionic neuron receives one very strong, always suprathreshold, nicotinic synapse denoted as primary and a variable number (n) of weak nicotinic synapses denoted as secondary. In many instances, summation between pairs of secondary EPSPs is sufficient to trigger an action potential. Due to this synaptic arrangement, the spike output of postganglionic neurons reflects the activity of primary synapses combined with that driven by suprathreshold coincidences between subthreshold secondary EPSPs. The $n + 1$ rule describes nicotinic convergence in bullfrog sympathetic ganglia (Dodd and Horn 1983; Karila and Horn 2000) and also seems to operate in mammalian sympathetic ganglia (Hirst and McLachlan 1986; Jänig and McLachlan 1992; Skok and Ivanov 1983).

POSTULATE 2—ENTIRE POPULATIONS OF AUTONOMIC NEURONS ARE UNIFORM IN THEIR SYNAPTIC ORGANIZATION. Functional subsets of ganglionic neurons can be differentiated by their levels of secondary synaptic convergence (n) and by their selective expression of neuromodulatory mechanisms. For example, bullfrog secretomotor B-type sympathetic neurons have between one and three secondary synapses with a mean n of 1.2 (Karila and Horn 2000), and they selectively express an excitatory muscarinic synaptic mechanism (Smith and Weight 1986; Tosaka et al. 1968; Weight and Padjen 1973). As a consequence of uniformity within the B-cell population and the general lack of lateral interactions between postganglionic neurons, one can infer population behavior of this cell type from that of a single neuron, thus simplifying the design of simulations and experiments. Using this approach, it also becomes possible to compare integration in subpopulations of sympathetic and parasympathetic neurons that differ in their synaptic organization. Such variations appear to reflect the phenotypic specialization of ganglionic neuronal subtypes that control different target tissues and the evolutionary adaptation of homologous ganglia from different vertebrate species (Gibbins 1995; Gibbins et al. 2000; Purves et al. 1986).

POSTULATE 3—PREGANGLIONIC NEURONAL ACTIVITY IS GENERATED BY A POISSON PROCESS IN WHICH THE TIME INTERVALS BETWEEN SYNAPTIC EVENTS ARE EXPONENTIALLY DISTRIBUTED. Postganglionic firing in anesthetized animals and awake humans is characteristically very irregular (Macefield et al. 2002; McAllen and Malpas 1997). In cases where the pattern of presynaptic activity has been recorded intracellularly from postganglionic neurons in vivo, the noisy intervals between synaptic events can be approximated by an exponential distribution (see Fig. 5A2 in McLachlan et al. 1998 and Fig. 4A in Häbler et al. 1999). By idealizing presynaptic activity as a Poisson process, one can mathematically model the occurrence of synaptic events.

Computational modeling

All simulations of synaptic activity followed the multi-step process outlined in Fig. 1A. In this procedure, templates of synaptic conductance were constructed by first determining the timing of primary and secondary nicotinic events. For each event, an appropriately sized postsynaptic conductance waveform was added to the template. Finally, the completed template was used to drive the conductance-based model sympathetic neuron by numerically integrating the underlying system of ordinary differential equations.

Timing of synaptic events was determined by repeatedly drawing a random number (0–1) and comparing it with P_{syn}, the probability of an event occurring during a specified time window (t_{win}). If the random number was $\leq P_{syn}$, an event was added to the template. For a Poisson process governing the timing of n identical synapses, $P_{syn}(t \leq t_{win}) = 1 - \exp(-nf_{pre}t_{win})$ (Colquhoun 1971). The value of t_{win}, which also signifies the temporal resolution of the saved data, was set to 0.25 ms for numerical simulations and to 0.05 ms for templates used in dynamic-clamp experiments. The equation for P_{syn} permitted us to simulate the generation of synaptic events by nonintegral as well as integral numbers of synapses. For example, in Fig. 4A, synaptic gain was calculated for n's of 1.2, 3, and 9 to model the average convergence levels associated with cellular populations of bullfrog B and C neurons and rat sympathetic neurons.

The time course of the fast nicotinic synaptic conductance (g_{syn}) was derived by fitting a synaptic current, recorded from a B neuron under two-electrode voltage clamp, to the sum of two exponentials and scaling it to a peak amplitude of 1 (see Fig. 2A in Schobesberger et al. 2000). The time constants were 1 ms for the rise and 5 ms for the decay. Unless stated otherwise, the strengths of nicotinic synapses were adjusted by scaling the unitary template to $\bar{g}_{syn} = 100$ nS for primary synapses and 9.61 nS for secondary synapses. The latter represents 90% of threshold-g_{syn}, the nicotinic conductance required

to depolarize the resting model to threshold for generating an action potential (Schobesberger et al. 2000).

Other conductances in the model sympathetic B neuron have already been described (Schobesberger et al. 2000). They include a fast inactivating sodium conductance (g_{Na}), a noninactivating delayed-rectifier potassium conductance (g_{K}), an M-type potassium conductance (g_{M}), a cyclic nucleotide-gated cation leak conductance (g_{CNG}), and a voltage-insensitive background leak conductance (g_{leak}). These are sufficient to produce a realistic resting potential, steady-state current-voltage relation, and spike threshold. For all simulations, $\bar{g}_{Na} = 800$ nS, $\bar{g}_{K} = 2,000$ nS, $g_{leak} = 3$ nS, $E_{Na} = 60$ mV, $E_{K} = -90$ mV, $E_{leak} = -40$ mV, $E_{M} = -90$ mV, $E_{CNG} = 0$ mV, $E_{syn} = 0$ mV, and the membrane capacitance was 100 pF. For simulations of muscarinic and peptidergic excitation, $\bar{g}_{M}$ and g_{CNG} were adjusted from resting values of 40 and 0 to 30 and 4 nS. See the supplemental material[1] for a full listing of the equations describing each ionic conductance.

In one set of simulations, presynaptic facilitation of nicotinic synapses was modeled as an additive process followed by exponential decay. In the presence of facilitation, each presynaptic event transiently increased the amplitudes (*A*) of all successive events by a factor having the following form: $A = 1 + 2 \exp(-t/\tau_{decay})$. The magnitude of facilitation (2) and the range of τ_{decay} (12–50 ms) were chosen to reproduce experimental data from bullfrog B neurons (Shen and Horn 1995).

Software implementation of simulations

Computational simulations employed programs written in MATLAB R11–13 (MathWorks, Natick, MA) using ode15s, a stiff variable-step differential-equation solver, and a personal computer. Our software, collectively called NEUROSIM, is freely available and can be obtained by contacting the authors. The voltage data and activation/ inactivation parameter values from each simulation were saved every 0.25 ms. Simulating 20–4,000 s of neural activity for each measurement of synaptic gain required between 2 and 100 h of real time. Illustrations were drafted with Igor Pro 4.0 (PC Edition, WaveMetrics, Lake Oswego, OR).

Cell culture

Paravertebral sympathetic ganglia 8–10 were dissected from pithed adult bullfrogs (*Rana catesbeiana*, 4–6 in) using a protocol approved by the University of Pittsburgh's Institutional Animal Care and Use Committee. The ganglia were desheathed, minced, and dissociated by incubation in Ringer containing 300 μg/ml Liberase Blendzyme 3 (Roche Diagnostics, Indianapolis, IN) for 30–60 min at 32°C, followed by mechanical trituration with graded fire-polished Pasteur pipettes. Ringer contained (in mM) 115 NaCl, 2 KCl, 1.8 CaCl$_2$, and 4 NaHEPES, adjusted to pH 7.3. After centrifugation and resuspension in culture medium, the dissociated cells were plated onto glass coverslips coated with poly-D-lysine (BD Biosciences, Bedford, MA). Cell cultures were maintained for ≤ 2 wk in diluted L-15 medium (65%) supplemented with 5 mM dextrose, 2 mM L-glutamine, 1 mM CaCl$_2$, 5% fetal bovine serum, 100 U/ml penicillin, and 100 μg/ml streptomycin.

Perforated-patch clamp recording and dynamic clamp

Whole cell perforated-patch recordings were made at room temperature from neurons visualized on an inverted microscope. Fire-polished patch pipettes were filled with internal solution containing (in mM) 110 K$^+$-gluconate, 10 NaCl, and 5 NaHEPES, adjusted to pH 7.1 with HCl. Stock solution of amphotericin-B (Sigma; 25 mg/ml in

dimethyl sulfoxide) was added to the internal solution to a final concentration of 250 μg/ml. With pipette resistances of 2–5 MΩ, this amphotericin-B concentration typically resulted in final access resistances of 5–10 MΩ, after 30–60 min of recording. Access resistance was monitored throughout the experiment and compensated using the bridge circuitry of the recording amplifier. The external recording solution consisted of Ringer as described above.

The dynamic current-clamp method was used to record membrane potential and create virtual nicotinic synapses. For this purpose, we used G-clamp (Kullmann et al. 2004), which includes an AxoClamp 2B amplifier (Axon Instruments, Union City, CA), G-clamp software written in the LabVIEW-RT programming environment (National Instruments, Austin, TX), a standard Windows-based computer, an embedded controller running under a real-time operating system (National Instruments), and a multifunction I/O board for data acquisition and signal generation (PXI-6052E, National Instruments). This system has the ability to read data files containing conductance templates of synaptic activity identical to those used in the numerical simulations (Fig. 1*A*). These templates were used to stimulate neurons while measuring and storing their membrane potential responses and the currents injected by the clamp. The dynamic clamp's real-time loop speed and data sampling rate were both 20 kHz.

Recordings were made from the largest cells because they are generally B neurons (Dodd and Horn 1983; Jan and Jan 1982). Once patch perforation by amphotericin-B had reduced access resistance to 15 MΩ or less, we began measuring threshold-g_{syn}. When a stable estimate was obtained, this value was used to scale a synaptic conductance template for measuring synaptic gain. Because execution of a synaptic conductance template could transiently alter postsynaptic excitability for several minutes, we continually measured threshold-g_{syn} between trials, waiting until it stabilized again before execution of the next synaptic conductance template. Steady-state *I-V* relations were measured repeatedly throughout each experiment to monitor leak resistance.

Analysis of synaptic gain and the associated errors

Synaptic gain (*G*) was calculated by dividing the number of postsynaptic action potentials in a given trial by the average number of presynaptic events per synapse. To estimate the errors associated with counts of postsynaptic action potentials and with estimates of *G*, we assumed that postsynaptic activity was generated by an inhomogeneous Poisson process (Berry and Meister 1998). The inhomogeneity arose from filtering of short interspike intervals at high stimulus frequencies (Fig. 3*A*). For all Poisson processes, the mean number of events (μ) equals the total number of events generated, and the CV = $1/\sqrt{\mu}$ (Colquhoun 1971). We therefore adjusted the duration of simulations to produce ~400 postsynaptic action potentials to obtain a CV or "counting error" of ~5%. The error in *G*, which depends on the count of presynaptic and postsynaptic spikes, was estimated as $CV_G \approx \sqrt{CV_{post}^2 + CV_{pre}^2}$ (Colquhoun 1971). The SD of *G* can be calculated as $\sigma_G = CV_G G$. Since a single simulation was used to calculate each value of *G*, the SE equals σ_G. All errors in *G* are plotted or reported as $\pm$SE.

In dynamic-clamp experiments, shorter templates of 200 events per synapse were employed so that the data could be collected from a stable recording in <1 h. Grouped data from these experiments are reported as the means $\pm$ SE. In statistical comparisons, the criterion for significance was $P < 0.05$.

RESULTS

Frequency dependence of synaptic gain

To examine how the presynaptic firing frequency controls gain, templates of synaptic activity were constructed and used to stimulate a model sympathetic neuron (Fig. 1*A*). Each

---

[1] The supplementary material is available online at http://jn.physiology.org/ cgi/content/full/00470.2004/DC1.
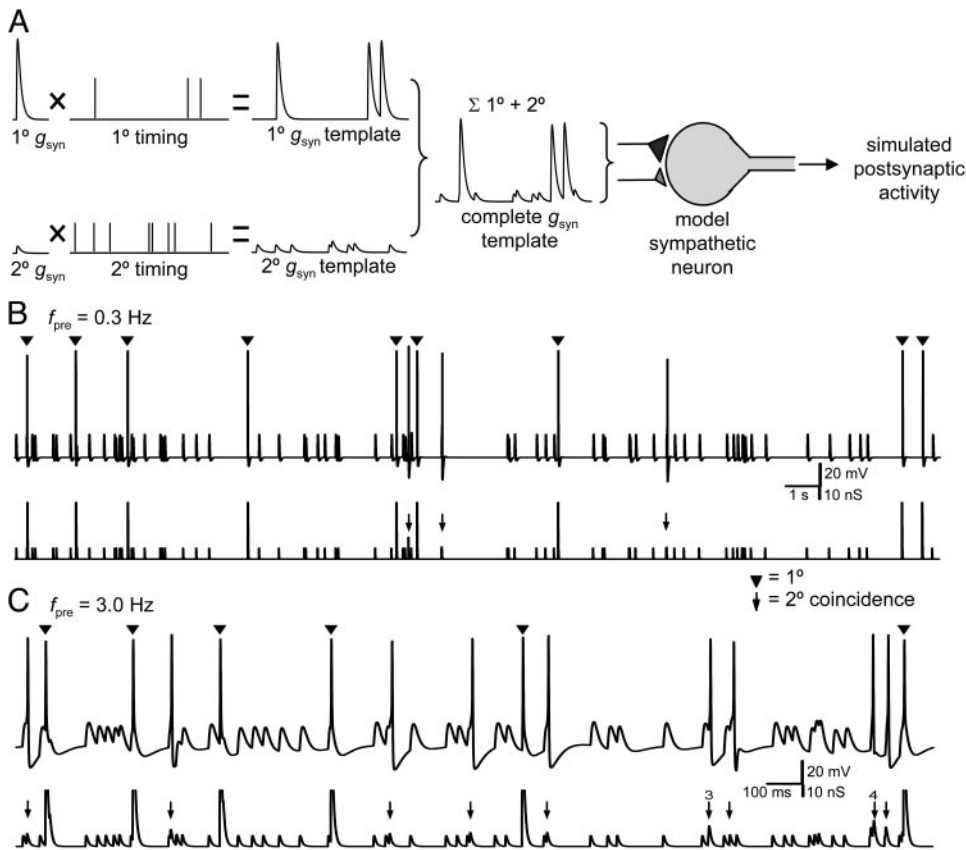
FIG. 1. Design and appearance of synaptic-gain simulations. *A*: all simulations were conducted in 2 steps, beginning with assembly of a synaptic-conductance template and ending with numerical integration of the model. The conductance template for a particular mean presynaptic frequency (f_{pre}) had 1 component for primary (1°) events and another for secondary (2°) events. Appropriately scaled conductance waveforms were added to the template at times determined by the Poisson process used to model synaptic activity. The completed template describing the entire pattern of activity for $n + 1$ synapses was used to drive the conductance-based model. *B* and *C*: examples of conductance templates (*bottom*) and resulting postsynaptic membrane potentials (*top*) at 2 different levels of presynaptic activity. In response to presynaptic stimulation at 0.3 Hz (*B*), most (9/12) postsynaptic action potentials were driven by primary excitatory postsynapatic potentials (EPSPs). With 3-Hz stimulation (*C*), most (9/15) postsynaptic action potentials were triggered by temporal suprathreshold coincidences between secondary EPSPs rather than by primary EPSPs. The vast majority of secondary coincidences were binary. Two rare examples of a triple and a quadruple coincidence are labeled with numbers.

synaptic template incorporated information about the number of converging nicotinic synapses, their strength, and their temporal pattern of activity. We began by considering a case with one primary synapse and nine secondary synapses, an $n + 1$ arrangement similar to that observed in the rat superior cervical ganglion (Purves et al. 1986). The strength of each secondary nicotinic synapse was set to 9.61 nS, which is 90% of threshold-g_{syn}. The temporal pattern of synaptic events was created by assuming presynaptic activity arises from a Poisson process. By combining the timing information with appropriately scaled synaptic conductance waveforms, a complete template was constructed that described the time course of total synaptic conductance over an entire simulation. The membrane potential response to synaptic stimulation was computed by numerically integrating the Hodgkin-Huxley system of equations (see supplemental material for a full listing) that describe the model sympathetic neuron (Fig. 1, *B* and *C*).

The efficacy of secondary synapses and their ability to generate gain varied with the presynaptic frequency. In response to stimulation at 0.3 Hz, most postsynaptic action potentials were driven in one-to-one fashion by primary EPSPs (Fig. 1*B*). In contrast, setting the presynaptic frequency to 3 Hz changed the outcome so that most postsynaptic firing was driven by secondary synapses (Fig. 1*C*). Inspection of the records revealed that virtually all of the spikes triggered by secondary EPSPs resulted from binary coincidences. At 3 Hz, there were occasional triple and quadruple coincidences, but they had little impact on the overall rate of postsynaptic firing (Fig. 1*C*). These effects of activity on synaptic gain can be understood more easily by considering a simpler case with only three synapses (Fig. 2*A*). In this schematic illustration, all three

presynaptic inputs fire an average of four times, and the postsynaptic cell responds by firing seven times, thus resulting in a gain of 1.75. Four of the action potentials (dark shading) originate from the primary synapse, while the remaining three (light shading) arise from temporal summation between secondary EPSPs. If the presynaptic frequency were increased in this example, the probability of secondary synaptic coincidences would also increase, eventually accounting for the majority of postsynaptic action potentials and a further increase in gain. On the other hand, reducing the presynaptic frequency would lessen the influence of secondary synapses, thereby causing gain to drop toward one.

To measure synaptic gain systematically as a function of mean presynaptic frequency, we drove the 9 + 1 model over a range of frequencies (0.1–20 Hz). The durations of these simulations were each adjusted to produce ≥400 postsynaptic spikes to reduce counting errors arising from the stochastic nature of the synaptic activity. The resulting relation shows that gain was a biphasic function of the mean presynaptic frequency (Fig. 2*B*), with a peak in the range of 2–5 Hz. The overall shape of the synaptic-gain relation constructed from the simulations was similar to that predicted by the more sparsely framed coincidence detection theory (Karila and Horn 2000), especially when the presynaptic frequency was <1 Hz (Fig. 2*B*). The main differences were observed at higher frequencies where the theory overestimated the peak gain and predicted an overly steep postpeak decline. We suspected these disparities were due to the different ways in which the two approaches introduce refractory periods that limit the rate of postsynaptic firing. For this purpose, the coincidence detection theory of Karila and Horn (2000) incorporates the arbitrary assumption
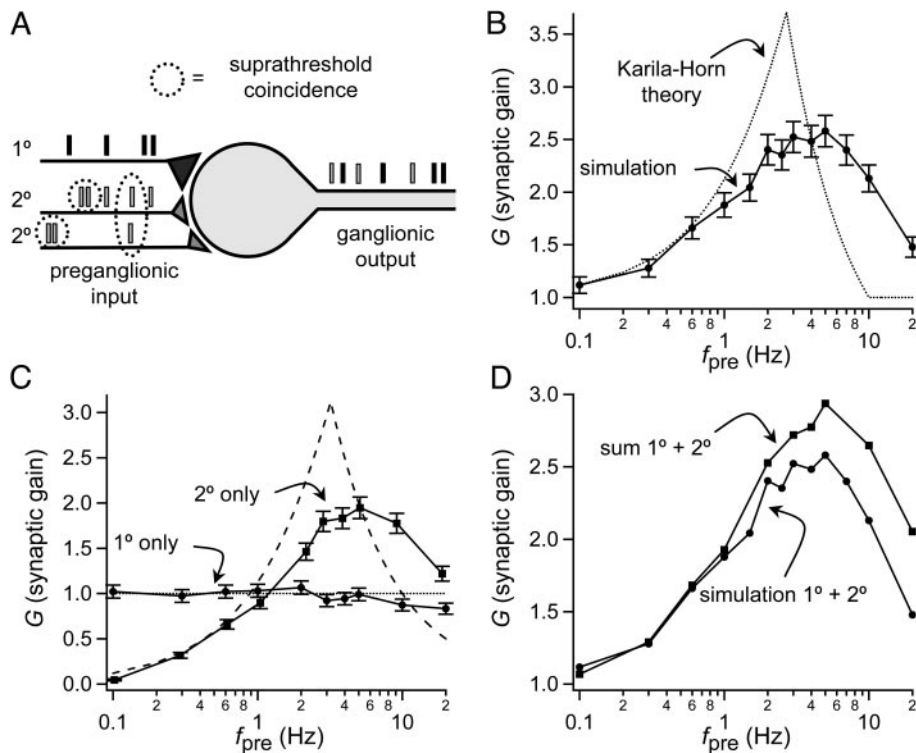
FIG. 2. Contributions of primary and secondary synapses to frequency-dependent synaptic gain. *A*: in an idealized schematic of $n + 1$ convergence ($n = 2$), each presynaptic neuron fires an average of 4 times. In response, the postsynaptic neuron fires 7 action potentials, 4 driven by primary (1°) EPSPs and 3 driven by coincidences between secondary (2°) EPSPs. The result is a synaptic gain of 1.75. *B*: comparison of the gain relation for $n + 1$ simulations ($n = 9$), and prediction of the coincidence detection theory of Karila and Horn (2000) reveals close agreement at lower presynaptic frequencies (f_{pre}) and a disparity at higher presynaptic rates. *C*: gain relations for a solitary primary synapse and for 9 secondary synapses in the absence of a primary synapse. The primary synapse has unitary gain, which begins to roll off when $f_{pre} > 5$ Hz. Dotted and dashed lines represent predictions of coincidence detection theory (Karila and Horn 2000). *D*: for presynaptic frequencies >1 Hz, the linear sum of the isolated gain responses (*C*) was greater than the response from the $n + 1$ simulations (*B*). This indicates that action potentials generated by primary EPSPs can occlude those driven by secondary synaptic activity. Error bars have been omitted for clarity.

that secondary EPSPs can only drive postsynaptic firing at a maximum rate of 10 Hz. In contrast, refractory properties of the model neuron emerge from its conductances and are not limited to spikes triggered by secondary EPSPs. Lowering the refractory cut-off frequency in the Karila and Horn (2000) theory reduced the peak of the gain relation but did not improve the overall fit to the simulation results (data not shown). To better understand the behavior of the conductance-based model, we therefore examined how primary and secondary EPSPs affect one another.

Interactions between primary and secondary synapses have consequences for gain

In addition to limiting the excitation produced by the summation of secondary EPSPs, one would expect refractory periods to introduce interactions between primary and secondary synapses. If, for example, a pair of secondary EPSPs coincided during or shortly after an action potential driven by a primary EPSP, the first action potential would prevent the second. To measure the extent of such effects, we first constructed separate gain relations to describe a single primary synapse and a group of nine secondary synapses (Fig. 2*C*). The gain of the solitary primary synapse was unitary at low stimulation rates, but decreased by ~17% when the presynaptic frequency was >10 Hz. This high-frequency roll-off suggests that refractory interactions between primary synaptic events can limit postsynaptic firing. In contrast, the gain relation for nine secondary synapses was biphasic, with a baseline that approached zero at lower frequencies, a peak of ~2.1 at 3–10 Hz, and a roll-off at higher rates. The high-frequency roll-off in this relation suggests that refractory mechanisms can also limit the efficacy of secondary synapses in the absence of a primary synapse.

To uncover interactions between primary and secondary synapses, we added the gain responses for isolated primary and secondary synapses and compared their sum with the gain relation describing combined $n + 1$ convergence (Fig. 2*D*). Although the two curves were similar when $f_{pre} < 1$ Hz, the summed gain response was greater than the combined gain response at higher frequencies. This indicates that interactions between primary and secondary synapses are minimal at low f_{pre}, but limit gain at higher stimulation rates.

Refractory periods alter postsynaptic spike timing

If postsynaptic refractoriness is responsible for the roll-off in synaptic gain at higher presynaptic frequencies (Fig. 2, *B–D*), frequency-dependent effects should be evident in the patterns of postsynaptic action potentials. This prediction was tested by constructing cumulative probability distributions of postsynaptic interspike intervals (Fig. 3*A*). When the presynaptic frequency was 0.6 Hz and gain was low, the distribution of postsynaptic interspike intervals was exponential, just like the distribution of presynaptic events. However, at higher presynaptic frequencies, the distributions of postsynaptic intervals fell short of the expected exponential relations. The disparity was clearest when the presynaptic firing rate was 20 Hz, which produced a large shortfall in postsynaptic interspike intervals <30 ms, with none <8 ms in duration. The lack of intervals <8 ms is also evident at the other presynaptic frequencies when the time scale of the distributions is expanded (Fig. 3*A*, *insets*).

To test whether refractory effects could account for the postsynaptic filtering effect, we measured two types of interactions. For pairs of primary EPSPs, the refractory period for production of an overshooting action potential was 8 ms (Fig. 3*B*). When the trailing stimulus was created by a pair of
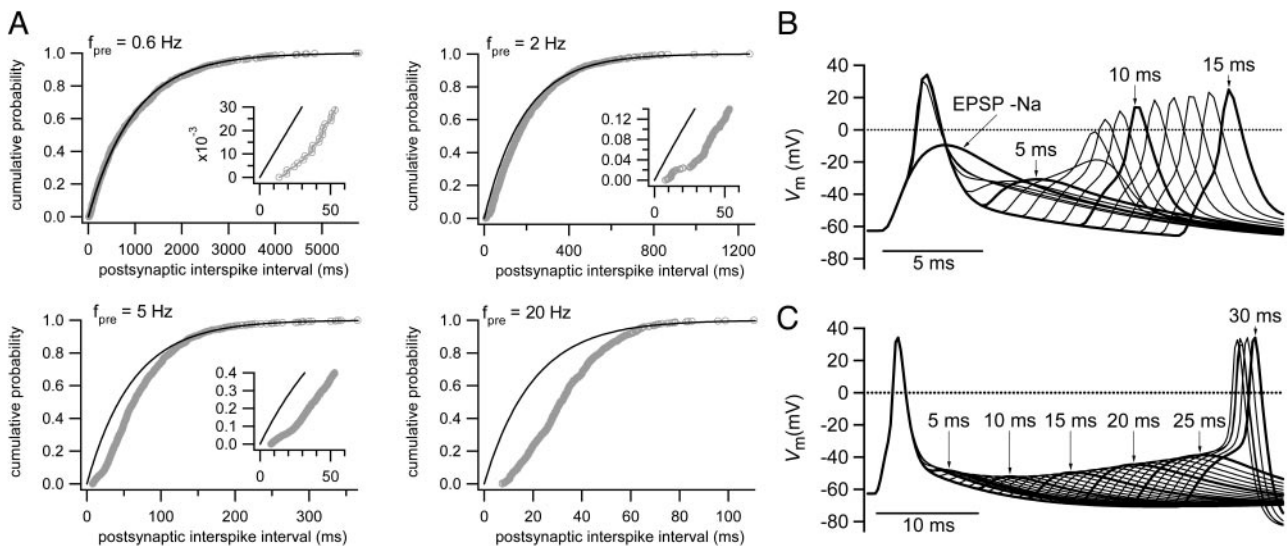
FIG. 3. Refractory periods alter the statistics of postsynaptic spike timing. *A*: cumulative probability histograms of postsynaptic interspike intervals (gray circles, data set from Fig. 2*B*) are described by exponential distributions (solid lines) for presynaptic activity when f_{pre} is low, but fall short when f_{pre} is high. Re-plotting the 1st 60 ms of the histograms (*insets*) shows that filtering of brief interspike intervals occurs at all values of f_{pre}, but becomes more prominent at higher f_{pre}, where brief intervals make up a greater proportion of all events. *B*: postsynaptic responses to pairs of primary (1°) EPSPs have a refractory period of 8 ms. The family of records includes 1 example simulated in the absence of the postsynaptic voltage-dependent sodium conductance (EPSP-Na). This trace shows the large amplitude of the primary EPSP used in these simulations. *C*: when the 2nd stimulus in a pair was created by 2 coincident secondary (2°) EPSPs (total $\bar{g}_{syn} = 180\%$ threshold-g_{syn}), the refractory period was 26 ms. Refractory periods shown in *B* and *C* correspond to the total filtering of interspike intervals <8 ms and the partial filtering of intervals <30 ms, effects that are most prominent during 20-Hz stimulation of the model (*A*).

simultaneous secondary EPSPs, which was much weaker than a primary EPSP, the refractory period was 26 ms (Fig. 3*C*). The brief refractory period between primary EPSPs explains the total absence of postsynaptic interspike intervals <8 ms (Fig. 3*A*), and it accounts for the roll-off in the gain relation of the isolated primary synapse (Fig. 2*C*). When the primary synapse was driven at 20 Hz, 13% of the intervals between EPSPs were <8 ms, which agrees well with the observed 17% reduction in gain. In contrast, the longer refractory period between primary and secondary EPSPs explains the partial filtering of postsynaptic interspike intervals <30 ms (Fig. 3*A*) and the roll-off of the gain relation for secondary synapses (Fig. 2*C*).

In the absence of refractory mechanisms, one would expect gain to increase as a monotonic function of the mean presynaptic frequency, saturating when gain is $n + 1$ (Karila and Horn 2000). We tested this prediction by counting the number of EPSPs separated by intervals that were <26 ms in the secondaries-only 20-Hz data. If all of these EPSPs had successfully triggered spikes, the gain would have been 9 rather than the observed 1.2. This agrees with the theoretical maximum for gain in the secondaries-only configuration, thereby supporting the conclusion that the refractory occlusion by secondary EPSPs causes most of the roll-off in the synaptic gain relation. In comparison, the effects of primary-primary synaptic occlusion (Fig. 2*C*) and primary-secondary synaptic occlusion (Fig. 2*D*) were relatively small.

Synaptic gain regulation by convergence and synaptic strength

Lowering secondary synaptic convergence to mimic the levels seen in sympathetic ganglia of amphibians and mice

($n = 1.2, 3$) (Karila and Horn 2000; Purves et al. 1986) caused a proportional reduction in maximum gain (Fig. 4*A*). Reducing secondary synaptic strength from 98 to 50% threshold-g_{syn}, while holding convergence constant at $n = 9$, showed that the peak of the gain relation also varied as a function of secondary synaptic strength (Fig. 4*B*).

Although the effects of convergence and synaptic strength on gain were generally consistent with the predictions of coincidence detection theory (Karila and Horn 2000), it was surprising to find G > 1 when secondary synaptic strength was set to 50% threshold-g_{syn} (Fig. 4*B*). This result contradicts the theory, which would require perfect coincidences between pairs of secondary EPSPs of this strength to generate action potentials. Since perfect coincidences are rare, the theory predicts there should be little or no gain above the baseline of 1 (Fig. 4*B*, dashed line). We examined this further by using even weaker synapses. For $f_{pre} = 5$ Hz and $n = 9$, $G = 1.31 \pm 0.06$ when secondary synaptic strength was 49% threshold-g_{syn} and $G = 1.17 \pm 0.05$ when secondary synaptic strength was 40% threshold-g_{syn}. The ability of sub-50% secondary EPSPs to trigger action potentials suggested it was very unlikely that binary coincidences were causing these effects. By examining the simulation records for triple, quadruple, and quintuple coincidences, we found that such higher order events accounted for 97–99% of the spikes driven by secondary synapses at 50, 49, and 40% threshold-g_{syn}.

Metabotropic modulation of synaptic gain

Metabotropic muscarinic excitation of sympathetic neurons operates through a branched signaling pathway that controls two ionic conductances. The better known is the M-type potassium conductance g_M, whose suppression dur-
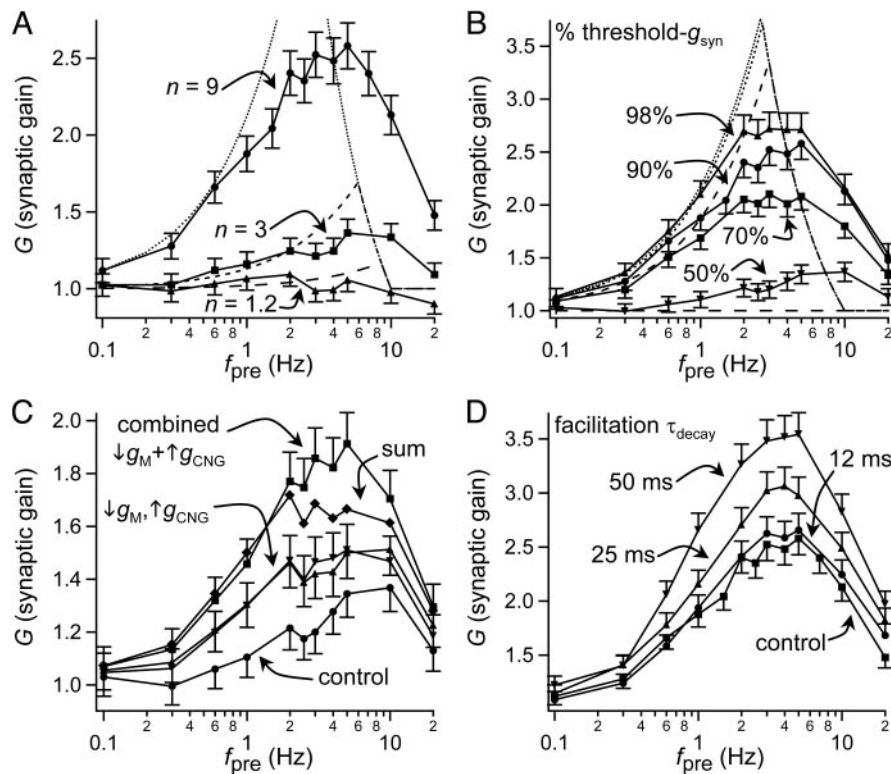
FIG. 4. Four factors that similarly alter the synaptic gain relation. *A*: as the number of secondary synapses (*n*) increased, synaptic gain was raised at all presynaptic frequencies (f_{pre}). *B*: increasing the strength of secondary synapses also elevated gain across the f_{pre} spectrum. Dashed lines in *A* and *B* are gain relations calculated from coincidence-detection theory (Karila and Horn 2000) using corresponding temporal windows of suprathreshold summation that were measured with the conductance-based model (Schobesberger et al. 2000). See text for explanation of these comparisons. *C*: branched pathway that mediates muscarinic and peptidergic excitation ($\bar{g}_M = 40 \to 30$ nS, $g_{CNG} = 0 \to 4$ nS) caused a synergistic increase in synaptic gain. In this family of gain relations, secondary $\bar{g}_{syn} = 50\%$ threshold-g_{syn}. *D*: adding presynaptic facilitation to the model also increased the magnitude of synaptic gain at most presynaptic frequencies. Effect of facilitation was enhanced when longer decay rates were used for the facilitation factor.

ing synaptic stimulation of muscarinic receptors by acetylcholine produces a slow EPSP that can last for tens of seconds (Adams et al. 1982; Smith 1994; Tosaka et al. 1968). In addition, muscarinic receptors activate a second membrane current that arises from a nonselective cation conductance (Tsuji and Kuba 1988). Schobesberger et al. (2000) suggested that the cation conductance is gated by cyclic nucleotides (g_{CNG}) and went on to show through simulations that g_{CNG} and g_M can act alone or together to increase the effective strength of subthreshold nicotinic EPSPs. These findings imply that metabotropic excitation working through this and analogous pathways could serve to increase synaptic gain.

We tested this idea in simulations with nine secondary synapses set to a relatively weak resting level of 50% threshold-g_{syn}. Since the kinetics of muscarinic EPSPs are much slower than the time scale of nicotinic EPSPs and action potentials, metabotropic excitation was introduced by simply adjusting $\bar{g}_M$ from 40 to 30 nS and g_{CNG} from 0 to 4 nS. These modest conductance changes reflect the effects seen during muscarinic responses in sympathetic neurons (Tsuji and Kuba 1988). Altering $\bar{g}_M$ or g_{CNG} alone produced clear increases in synaptic gain at all but the very lowest frequencies of presynaptic stimulation (Fig. 4*C*). Changing both conductances together produced even larger increases. Comparing the sum of the individual effects with the combined responses reveals that the two components add linearly at lower presynaptic frequencies but combine synergistically between 2 and 10 Hz. These results are consistent with earlier experiments showing that g_M and g_{CNG} act in a supralinear way to alter the strength of nicotinic synapses and to increase the temporal window of summation between pairs of subthreshold EPSPs (Schobesberger et al. 2000).

Presynaptic facilitation increases synaptic gain

Mechanisms of presynaptic facilitation are widespread in autonomic ganglia. When facilitation was incorporated into synaptic templates, it increased synaptic gain at frequencies of 1–10 Hz (Fig. 4*D*). The exponential rate of decay of the presynaptic facilitation factor directly affected the magnitude of the gain response.

Experimental tests of computational predictions

The simulation results in the first part of this paper show how synaptic gain can arise as a use-dependent consequence of nicotinic synaptic convergence and be modulated by synaptic strength, metabotropic excitation, and presynaptic facilitation (Fig. 4). Evaluating the physiological significance of these findings requires that appropriate experimental tests be devised. Ideally, one would want to activate independently each of the synaptic inputs to an autonomic neuron with trains of asynchronous stimuli. Due to the impracticality of such an experiment, we adopted an alternative strategy of using the dynamic-clamp method to implement virtual nicotinic synapses on dissociated bullfrog B neurons. With this approach, one can compare how real B neurons and the model B neuron respond to identical patterns of synaptic stimulation. We began by measuring synaptic strength and the gain produced by $n + 1$ convergence.

Dynamic-clamp estimates of synaptic strength and gain

An automated binary search paradigm was used to measure the magnitude of virtual nicotinic synaptic conductance required to depolarize B neurons to threshold (Fig. 5). The procedure begins by testing boundary values that straddle
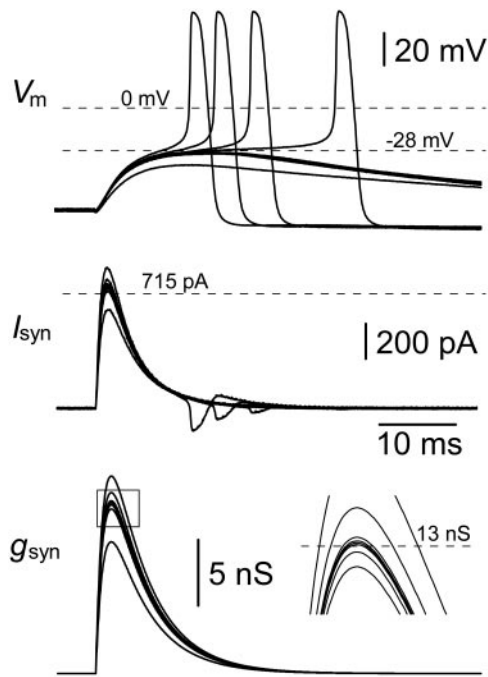
FIG. 5.   Measurement of the threshold synaptic conductance in a dissociated bullfrog sympathetic neuron. In this dynamic-clamp experiment, the magnitude of the synaptic conductance waveform was scaled between trials to find threshold-g_{syn} using a binary-search algorithm in G-clamp. This search strategy begins by testing the midpoint between 2 values for the peak conductance that straddle the threshold for generating an action potential. If the midpoint is subthreshold, the next point tested is halfway to the upper bound. If it is suprathreshold, the next point tested is halfway to the lower bound. Within 6–12 iterations of the cycle, the system settles at threshold-g_{syn}. In this example ($V_{rest} = -64$ mV, $R_{leak} = 1.22$ GΩ), G-clamp took 10 iterations to determine that threshold-g_{syn} was 13.0 nS. Each family of records includes dashed lines that denote the threshold values for V_m, I_{syn}, and g_{syn}. Note that the synaptic currents become outward (downward) when V_m overshoots and exceeds the reversal potential for I_{syn} (0 mV, dashed line).

threshold and homes in on a stable result within 8–12 trials (Kullmann et al. 2004). In a group of 12 neurons that were subsequently used for measurements of gain, we observed threshold-g_{syn} = 14.7 ± 1.7 nS (range, 7.0–23.7 nS), V_{rest} = –54.7 ± 3.0 mV (range, –40 to –70 mV), and R_{leak} = 739 ± 111 MΩ (range, 153 MΩ–1.48 GΩ). All of these cells had overshooting actions potentials. In comparison, the computational model assumed R_{leak} = 333 MΩ and predicted that threshold-g_{syn} = 10.68 nS and V_{rest} = –62.7 mV.

To measure the influence of secondary nicotinic EPSPs on synaptic gain, we constructed 5-Hz templates that were 40 s in duration and contained one primary synapse and zero, three, or nine secondary synapses. Five hertz was chosen as the presynaptic frequency because it generated maximal responses in gain simulations (Fig. 4A). After recording a value of threshold-g_{syn} that remained stable with repeated tests, the strength of secondary synapses in the stimulus templates was scaled to 90% threshold-g_{syn}, and the strength of the primary synapse was set at 10 times that of the secondary synapses. In cases where conditions drifted slowly over time, synaptic conductances were adjusted to maintain constant strength. Only cells in which at least two different levels of secondary convergence could be compared were included in the analysis. Figure 6 shows an example comparing convergence levels of three and nine secondary synapses. The *top traces* show dynamic-clamp recordings from one cell, and the *bottom traces* show simulated responses to the same synaptic templates using the computational model. From this example, three key points emerge. First, secondary synapses contributed to the spike output of the cell at both levels of convergence. As consequence of this effect, the gain produced in both cases was >1. Second, the contribution of secondary synapses was greater when $n = 9$ than when $n = 3$. This effect corresponds to greater convergence producing higher gain. Third, the pattern of spike output recorded from the B neuron was very well predicted by the computational simulations. In this example, only one spike is missing from the simulated output when $n = 3$ (Fig. 6A), and one spike is missing from the cellular output when $n = 9$ (Fig. 6B).

After calculating the gain produced by different levels of convergence, we made comparisons within cells and between groups of cells. Figure 7A shows an experiment in which it was possible to measure gain at three levels of n during 1 h of stable recording. Although stimulation with virtual synaptic activity caused transient changes in the resting potential and threshold-g_{syn}, these effects could not account for the fact that higher levels of convergence consistently and repeatedly produced higher levels of gain. In paired comparisons within individual cells, the gain produced by $n = 3$ (1.10 ± 0.03) was significantly greater than with $n = 0$ ($G = 0.93 ± 0.01$) in eight of eight cases ($P < 0.01$, nonparametric 2-tailed sign test). Similarly, the gain produced by $n = 9$ (1.42 ± 0.08) was significantly greater than with $n = 3$ in 11 of 11 cells ($P < 0.001$).
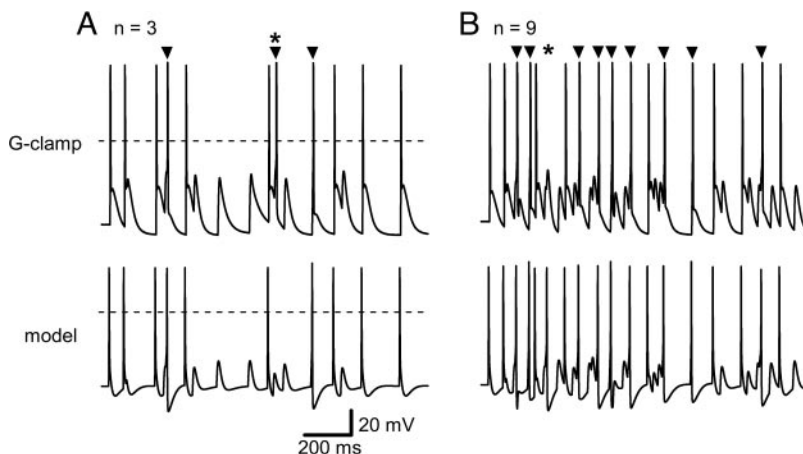

FIG. 6.   Virtual synaptic activity elicits similar firing patterns in sympathetic neurons and the computational model. Templates incorporating 3 secondary synapses (*A*) and 9 secondary synapses (*B*) were used to stimulate a neuron and the computational model. In each case, f_{pre} = 5 Hz, secondary synaptic strength = 90% threshold-g_{syn}, and primary synaptic strength = 900% threshold-g_{syn}. Note that with only 1 exception (*) for each template, the cell and model generated identical patterns of firing. The presence of action potentials driven by secondary synapses (▼) in both cases suggests gain >1. The greater contribution of secondary synapses to firing when $n = 9$ (*B*) than when $n = 3$ (*A*) indicates that higher convergence enhances gain.
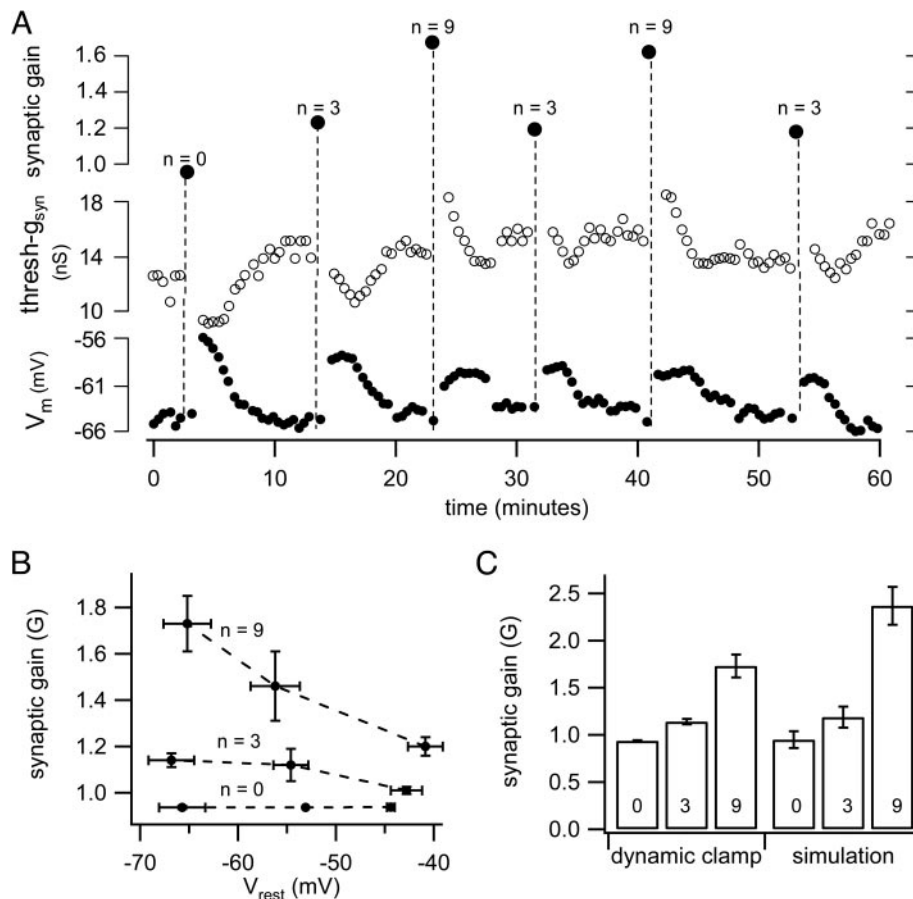
FIG. 7. Quantification of synaptic gain elicited in sympathetic neurons by different levels of convergence. *A*: time course of a dynamic-clamp experiment lasting 1 h. During this time, the cell was repeatedly stimulated with templates incorporating 0, 3, and 9 secondary synapses (f_{pre} = 5 Hz, secondary synaptic strength = 90% threshold-g_{syn}, primary synaptic strength = 900% threshold-g_{syn}). Each stimulus trial produced transient changes in threshold-g_{syn} and V_m, which were allowed to recover before the next trial. Higher convergence (*n*) led consistently to higher gain throughout the recording. *B*: grouped data describing synaptic gain from 11 cells. In each cell, at least 2 levels of gain were assessed with multiple interdigitated trials like that shown in *A*. When the gain data for each level of convergence was plotted as a function of the resting potential, it revealed a trend toward higher gain at hyperpolarized resting potentials that was absent when *n* = 0 and most evident when *n* = 9. *C*: comparing gain estimates from the most hyperpolarized resting potentials (re-plotted from *B*) with simulations using identical templates revealed similar results for *n* = 0 and 3. When *n* = 9, cellular estimates of gain fell short of the simulation data.

The magnitude of gain produced by one primary synapse alone (*n* = 0) and by three secondary synapses was very similar to that predicted by our simulations. In contrast, the gain observed with *n* = 9 was lower than predicted. To identify the possible origin of this disparity, we divided the cells into three groups based on their resting potentials (< -60, -60 to -50, and > -50 mV). Plotting the data in this way (Fig. 7*B*) revealed a voltage-dependence in gain that was most evident when *n* = 9. In the most hyperpolarized group of cells with *n* = 9, the disparity between cellular responses and simulations using the same templates was reduced but still evident (Fig. 7*C*).

Activity and calcium dependence of synaptic gain

Finding that gain could vary with resting potential (Fig. 7*B*) suggested that it might also change with activity. To test for such effects, the responses to 5-Hz stimulation were analyzed as four 10-s segments. This revealed that synaptic gain decreased over the course of individual trials when *n* = 9, but not when *n* = 3, and not in simulations. The decline was reversible when cells were given a few minutes rest between trials. When dynamic-clamp records and simulations from the last 10 s of stimulus trials were compared, secondary synapses failed to drive many of the spikes that were predicted by the simulations. This outcome differed from the close correspondence between recorded and simulated firing patterns at the beginning of the stimulus trial (Fig. 6*B*).

To document the use-dependent decline in gain more carefully and to examine its possible origin, we designed an experiment using a 40-s synaptic template (f_{pre} = 5 Hz, *n* = 9) consisting of 10 identical 4-s repeats. In a group of seven neurons ($V_{rest} = -63.1 \pm 3.1$ mV, threshold-$g_{syn} = 10.6 \pm 2.1$ nS, $R_{leak} = 732 \pm 84$ MΩ), the repeating template yielded an average gain of 1.64 ± 0.13 over the entire 40-s period. This was similar to the gain observed with the nonrepeating template (1.42), but lower than the gain (2.40 ± 0.19) produced in a simulation with the same template. The gain generated during each repeat declined gradually from a high of 2.00 ± 0.21 in the first 4 s to a low of 1.37 ± 0.09 in the last 4 s (7 cells). The time course of the decline in gain was similar when viewed for one cell (Fig. 8*A*) and for the group (Fig. 8*B*). By contrast, simulated voltage responses to the first and last segments of the repeating template were identical, with a gain of 2.40 ± 0.26.

We hypothesized that calcium entry was responsible for the observed reduction in synaptic gain. Indeed, the absence of calcium and calcium-activated potassium conductances in the computational model might account for the steady gain response seen in simulations with the 5-Hz repeating template. To test whether calcium entry mediates a reduction in synaptic gain, voltage-dependent calcium channels were blocked in the same group of seven cells using 10 μM Cd^{2+} (Jones and Marks 1989). Cadmium did not affect V_{rest} (-63.0 ± 3.3 mV; *P* = 0.86, paired *t*-test) or R_{leak} (761 ± 220 MΩ; *P* = 0.72, paired *t*-test), but caused significant increases in threshold-g_{syn} (13.3 ± 2.6 nS; *P* = 0.01, paired *t*-test) and in the average gain over the entire 40-s template (1.94 ± 0.17; *P* < 0.05, paired *t*-test; Fig. 8*C*). The overall changes in gain were also reflected in the 4-s repeats. Cadmium increased gain in the first 4-s
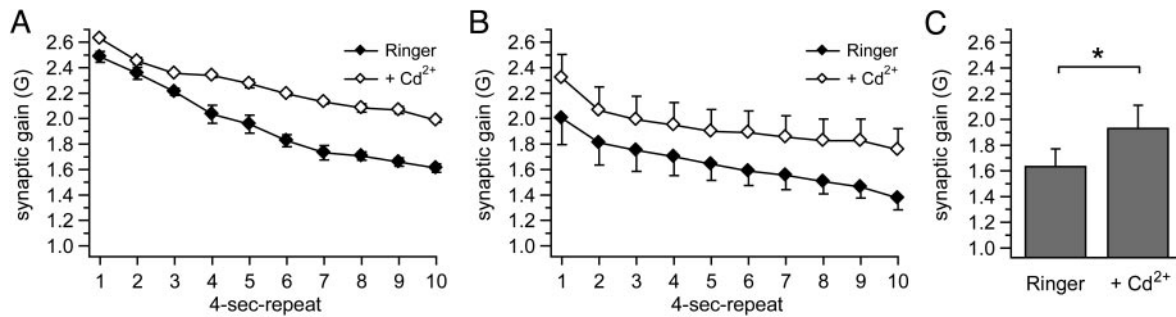
FIG. 8. Activity dependence and cadmium sensitivity of synaptic gain. A group of 7 cells was stimulated with a template containing 10 4-s repeats of identical virtual synaptic activity (f_{pre} = 5 Hz; n = 9). Each cell was stimulated several times with the template in normal Ringer and in Ringer containing 10 μM $CdCl_2$. A: averages of 3 trials from 1 cell. In normal Ringer, synaptic gain declined throughout the time course of stimulation. Adding cadmium to block voltage-dependent Ca^{2+} currents increased the initial value of gain and seems to attenuate the use-dependent decline. B: grouped data from 7 cells showing the same trends as in A. C: averaging gain data across the entire duration of the synaptic template shows that cadmium significantly increased the overall synaptic gain (7 neurons, $P < 0.05$, paired t-test).

period to 2.32 ± 0.19 and in the last 4-s period to 1.76 ± 0.16. These observations suggest that increased intracellular $[Ca^{2+}]$ may be partially responsible for the reduction in synaptic gain seen during prolonged synaptic stimulation.

DISCUSSION

Simulations define the general form of ganglionic gain in sympathetic ganglia

By simulating ganglionic integration with a conductance-based model, we have shown how the stereotypic $n + 1$ convergence pattern of fast nicotinic synapses found in para-vertebral sympathetic ganglia can serve to create a low-pass filter with unitary baseline gain and a high-frequency boost (Figs. 1, 2, and 9A). Plastic changes in several factors including convergence (Fig. 4A), secondary synaptic strength (Fig. 4B), metabotropic excitation (Fig. 4C), and presynaptic facilitation (Fig. 4D) are all capable of enhancing the filter's high-frequency boost. These findings show how the diversity in synaptic organization reported for subclasses of sympathetic neurons (Jänig 1995; Smith 1994) may provide a basis for specialized regulation of ganglionic gain. For example, vasomotor, secretomotor, and pilomotor sympathetic neurons may each have unique synaptic-gain functions that are optimized to drive their specific targets.

Quantitative limitations of coincidence-detection theory

The architecture of the conductance-based simulations followed from a much simpler coincidence-detection theory (Karila and Horn 2000) that rests on two basic ideas—preganglionic activity is noisy and pairs of secondary EPSPs can sum to reach threshold. Perhaps it is not surprising then that the theory successfully predicted the general form of gain relations produced by simulating $n + 1$ convergence and by simulating modulation through different types of synaptic plasticity (Figs. 2, B and C, and 4). Nonetheless, the theory consistently erred by predicting an overly sharp peak in the gain relation and an overly steep roll-off at high presynaptic frequencies. These effects arise from the theory's assumption that secondary synapses cannot drive firing at rates >10 Hz. In contrast to this hard cut-off, more complex refractory interactions emerge in the conductance-based model to control the peak value of gain

and its high-frequency roll-off (Fig. 3). The net effect of these refractory interactions is to produce a more gradual filtering of secondary synaptic events as a function of the presynaptic firing rate. In addition, the simulations with weak secondary synapses have shown that higher-order coincidences can influence firing (Fig. 4B). Using refractory filters having arbitrary sigmoidal shapes rather than step functions, we were able to fit closely the gain curves generated by simulations of the conductance-based model (data not shown). However, we were unable to modify the theory to incorporate these mechanisms in a form that could be derived on mechanistic grounds and that
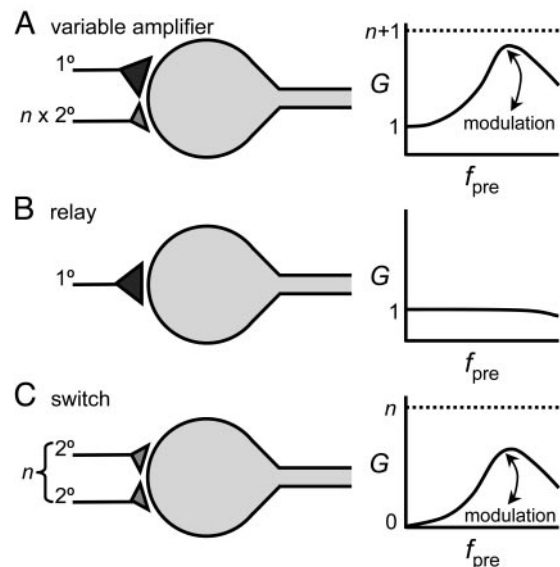

FIG. 9. Three generic forms of integration that arise from the innervation patterns observed in autonomic ganglia. A: $n + 1$ pattern of synaptic convergence seen in paravertebral sympathetic ganglia produces a variable synaptic amplifier whose gain function can be modulated by changes in the number and strength of secondary synapses, excitatory metabotropic synapses, and presynaptic facilitation. B: pattern of single innervation by 1 primary synapse enables some parasympathetic ganglia to behave as 1-to-1 relays. C: n pattern of synaptic convergence produces a synaptic gain function that behaves as a high-pass filter or switch. The ganglion only transmits preganglionic activity that is above a critical frequency. This pattern is found in some parasympathetic ganglia and in some prevertebral sympathetic ganglia. Given the nature of secondary synapses, the efficacy of this switch would also be subject to modulation.

would readily generalize to different conditions. One might expect such limitations to emerge, given that the underlying ordinary differential equations, based on the Hodgkin-Huxley formalism, are rarely susceptible to simple analytical solutions. In other words, coincidence-detection theory concisely captures the basic form, but not the exact form, of simulation results from the conductance-based model.

Insights from dynamic-clamp experiments

Even though the conductance-based model was designed to include many biophysical mechanisms, it omitted some details to achieve computational efficiency and to minimize the inclusion of arbitrary assumptions. For this reason, it was important to compare the responses of living neurons to the computational results. By taking such an approach, one can critically evaluate the model and focus attention on mechanisms that need further scrutiny.

The dynamic-clamp data show that the model correctly predicted the magnitude threshold-g_{syn} for nicotinic excitation and the effect of secondary synaptic convergence on synaptic gain during 5-Hz stimulation. In contrast, the model did not predict the activity dependence of synaptic gain, as revealed at $n = 9$ by the apparent correlation with resting potential (Fig. 7B) and by the decline in gain during the course of single stimulus trials (Fig. 8, A and B). Treating cells with 10 μM Cd^{2+} raised the level of gain during the first 4 s of stimulation ($f_{pre} = 5$ Hz, $n = 9$) from 2.00 ± 0.21 to 2.32 ± 0.19, which is close to the level of 2.40 ± 0.26 predicted by the model. Cadmium also appeared to decrease, but not eliminate, the decline of gain (Fig. 8A). Although these results indicate that calcium-dependent processes play a role in the regulation of gain, they cannot fully account for the use-dependent decline observed during 5-Hz stimulation and should therefore be interpreted with caution. Within our records, we also looked for, but were unable to detect obvious changes in spike threshold and morphology (upstroke, peak, repolarization) that could account for the decrease in gain during stimulation. Solving this problem will require further experimental analysis.

Function follows form: other autonomic ganglia and brain relays

Outside of the paravertebral sympathetic system, the different patterns of convergence seen in other ganglia can now be interpreted, based on our results. In the simplest pattern, postganglionic neurons are innervated by one primary nicotinic synapse. This arrangement occurs in the rat parasympathetic submandibular ganglion (Lichtman 1980), which controls salivation, and in the frog parasympathetic cardiac ganglion (Dennis et al. 1971), which modulates contractions of the heart. In our model, neurons with this innervation pattern behave as 1:1 relays that roll off at higher presynaptic frequencies (Figs. 2C and 9B). In another motif, characterized by the absence of a primary synapse and the presence of multiple secondary synapses, autonomic neurons behave as a band-pass filter (Figs. 2C and 9C). This organization enables the parasympathetic pelvic ganglion in the cat to perform as an ON-OFF switch during the micturition reflex (DeGroat and Saum 1976), which gates filling and emptying of the bladder. A similar convergence pattern also exists in a subpopulation of neurons in the

guinea-pig celiac ganglion (Gibbins et al. 2003; McLachlan and Meckler 1989). These prevertebral sympathetic neurons, which receive both preganglionic and intestinofugal inputs (Gibbins et al. 2003), exert a modulatory gating influence on gastrointestinal motility, secretions, and blood flow (Furness and Costa 1987).

The levels of convergence seen in autonomic ganglia are sparse compared with the massive convergence found on cortical pyramidal cells, cerebellar Purkinje cells, and spinal motoneurons. However, sparse convergence operates in many brain nuclei that are traditionally viewed, like autonomic ganglia, as synaptic relays. Perhaps the best example is the lateral geniculate nucleus (LGN). Simultaneous recordings between retinal ganglion cells and the LGN have revealed that LGN neurons receive excitatory input from fewer than six ganglion cells (Mastronarde 1992), and these connections are characterized as strong or weak (Usrey et al. 1999). Our approach may therefore have relevance to other circuits with sparse convergence.

Importance of gain in autonomic negative-feedback loops

Negative-feedback loops are critical elements of physiological control processes, including those mediated by the neuroendocrine and autonomic systems (Khoo 2000). The functional gain that emerges as an inherent component of a negative-feedback loop leads to faster and more accurate homeostatic control (Scher 1989; Scher et al. 1991). An important example of this mechanism arises in the baroreceptor reflex, an important focal point for neural control of the circulation (Scher et al. 1991). The reflex allows blood pressure to be maintained within a relatively narrow range despite changes in body posture and cardiac output. In the process, afferent feedback from sensory receptors regulates the output of motor activity in the sympathetic and parasympathetic systems, ultimately leading to changes in cardiac function and vascular tone. Despite extensive study of the baroreceptor reflex, the neural origin of its gain remains unclear. Much of the focus has centered on synapses in the nucleus tractus solitarius and the rostral ventral lateral medulla (Dampney 1994; Sun 1995), but relatively little attention has been paid to the potential contributions of synapses in the spinal cord, in sympathetic ganglia, and at neuroeffectors to the overall gain of the reflex. We propose that synaptic gain in the baroreceptor reflex may be distributed throughout much of the circuit, including sympathetic ganglia, rather than being confined to one or two anatomical loci.

In vivo evidence of synaptic gain in paravertebral sympathetic ganglia

Our results indicate that synaptic gain rises above one when secondary synapses help to drive postganglionic firing. Evidence for such behavior under physiological conditions comes from in vivo intracellular recordings in the mouse, guinea pig, hamster, rabbit, rat, and bullfrog (Häbler et al. 1999; Ivanoff and Smith 1995; Ivanov and Purves 1989; McLachlan et al. 1997, 1998; Skok and Ivanov 1983). The data from these studies of paravertebral sympathetic neurons provide evidence that primary and secondary nicotinic synapses generally form an $n + 1$ pattern of convergence. In several instances, the

morphology of the spike afterhyperpolarization has been used to identify which class of synapses triggers individual action potentials. Using this approach, it is clear that secondary synapses play a role in driving postganglionic activity. For examples, see Fig. 1*B* in Skok and Ivanov (1983), Fig. 1*A* in McLachlan et al. (1998), Fig. 4 in Ivanoff and Smith (1995), and Fig. 3 in McLachlan (2003). Additional evidence for synaptic gain comes from the observation that average rates of subthreshold and suprathreshold synaptic events are very similar in a range of mammals (see Table 2 in Ivanov and Purves 1989). When convergence is taken into account, these data indicate that individual postganglionic neurons fire at higher frequencies than preganglionic neurons. When viewed in the context of our model (Fig. 2*A*), this means that amplification is a common integrative feature of sympathetic ganglia.

REFERENCES

Adams PR, Brown DA, and Constanti A. M-currents and other potassium currents in bullfrog sympathetic neurones. *J Physiol* 330: 537–572, 1982.
Akasu T and Nishimura T. Synaptic transmission and function of parasympathetic ganglia. *Prog Neurobiol* 45: 459–522, 1995.
Berry MJ and Meister M. Refractoriness and neural precision. *J Neurosci* 18: 2200–2211, 1998.
Colquhoun D. *Lectures on Biostatistics—An Introduction to Statistics with Applications in Biology and Medicine.* Oxford, UK: Clarendon Press, 1971.
Dampney RA. Functional organization of central pathways regulating the cardiovascular system. *Physiol Rev* 74: 323–364, 1994.
DeGroat WC and Saum WR. Synaptic transmission in parasympathetic ganglia in the urinary bladder of the cat. *J Physiol* 256: 137–158, 1976.
Dennis MJ, Harris AJ, and Kuffler SW. Synaptic transmission and its duplication by focally applied acetylcholine in parasympathetic neurons in the heart of the frog. *Proc R Soc Lond B Biol Sci* 177: 509–539, 1971.
Dodd J and Horn JP. A reclassification of B and C neurones in the ninth and tenth paravertebral sympathetic ganglia of the bullfrog. *J Physiol* 334: 255–269, 1983.
Furness JB and Costa M. *The Enteric Nervous System.* Edinburgh: Churchill Livingstone, 1987.
Gibbins I. Chemical neuroanatomy of sympathetic ganglia. In: *Autonomic Ganglia*, edited by McLachlan EM. Australia: Harwood Academic Publishers, 1995, p. 73–121.
Gibbins IL, Jobling P, Messenger JP, Teo EH, and Morris JL. Neuronal morphology and the synaptic organisation of sympathetic ganglia. *J Auton Nerv Syst* 81: 104–109, 2000.
Gibbins IL, Teo EH, Jobling P, and Morris JL. Synaptic density, convergence, and dendritic complexity of prevertebral sympathetic neurons. *J Comp Neurol* 455: 285–298, 2003.
Häbler HJ, McLachlan EM, Jamieson J, and Davies PJ. Synaptic responses evoked by lower urinary tract stimulation in superior cervical ganglion cells in the rat. *J Urol* 161: 1666–1671, 1999.
Hirst GD and McLachlan EM. Development of dendritic calcium currents in ganglion cells of the rat lower lumbar sympathetic chain. *J Physiol* 377: 349–368, 1986.
Ivanoff AY and Smith PA. In vivo activity of B- and C-neurones in the paravertebral sympathetic ganglia of the bullfrog. *J Physiol* 485: 797–815, 1995.
Ivanov A and Purves D. Ongoing electrical activity of superior cervical ganglion cells in mammals of different size. *J Comp Neurol* 284: 398–404, 1989.

Iversen S, Iversen L, and Saper CB. The autonomic nervous system and the hypothalamus. In: *Principles of Neural Science* (4th ed.), edited by Kandel ER, Schwartz JH, and Jessell TM. New York: McGraw-Hill, 2000, p. 962–981.
Jan LY and Jan YN. Peptidergic transmission in sympathetic ganglia of the frog. *J Physiol* 327: 219–246, 1982.
Jänig W and McLachlan EM. Characteristics of function-specific pathways in the sympathetic nervous system. *Trends Neurosci* 15: 475–481, 1992.
Jänig WM. Ganglion transmission *in vivo*. In: *Autonomic Ganglia*, edited by McLachlan EM. Luxembourg City, Luxembourg: Harwood, 1995, p. 349–395.
Jones SW and Marks TN. Calcium currents in bullfrog sympathetic neurons. I. Activation kinetics and pharmacology. *J Gen Physiol* 94: 151–167, 1989.
Karila P and Horn JP. Secondary nicotinic synapses on sympathetic B neurons and their putative role in ganglionic amplification of activity. *J Neurosci* 20: 908–918, 2000.
Khoo MCK. *Physiological Control Systems.* Piscataway, NJ: IEEE Press, 2000.
Kuba K and Koketsu K. Synaptic events in sympathetic ganglia. *Prog Neurobiol* 11: 77–169, 1978.
Kullmann PHM, Wheeler DW, Beacom J, and Horn JP. Implementation of a fast 16-bit dynamic clamp using LabVIEW-RT. *J Neurophysiol* 91: 542–554, 2004.
Lichtman JW. On the predominantly single innervation of submandibular ganglion cells in the rat. *J Physiol* 302: 121–130, 1980.
Macefield VG, Elam M, and Wallin BG. Firing properties of single postganglionic sympathetic neurones recorded in awake human subjects. *Auton Neurosci* 95: 146–159, 2002.
Mastronarde DN. Nonlagged relay cells and interneurons in the cat lateral geniculate nucleus: receptive-field properties and retinal inputs. *Vis Neurosci* 8: 407–441, 1992.
McAllen RM and Malpas SC. Sympathetic burst activity: characteristics and significance. *Clin Exp Pharmacol Physiol* 24: 791–799, 1997.
McLachlan EM. Transmission of signals through sympathetic ganglia–modulation, integration or simply distribution? *Acta Physiol Scand* 177: 227–235, 2003.
McLachlan EM, Davies PJ, Häbler HJ, and Jamieson J. On-going and reflex synaptic events in rat superior cervical ganglion cells. *J Physiol* 501: 165–181, 1997.
McLachlan EM, Häbler H-J, Jamieson J, and Davies PJ. Analysis of the periodicity of synaptic events in neurones in the superior cervical ganglion of anaesthetized rats. *J Physiol* 511: 461–478, 1998.
McLachlan EM and Meckler RL. Characteristics of synaptic input to three classes of sympathetic neurone in the coeliac ganglion of the guinea-pig. *J Physiol* 415: 109–129, 1989.
Powley TL. Central control of autonomic functions: organization of the autonomic nervous system. In: *Fundamental Neuroscience* (2nd ed.), edited by Squire LR, Bloom FE, McConnell SK, Roberts JL, Spitzer NC, and Zigmond MJ. San Diego: Academic Press, 2003, p. 911–933.
Purves D, Rubin E, Snider WD, and Lichtman J. Relation of animal size to convergence, divergence, and neuronal number in peripheral sympathetic pathways. *J Neurosci* 6: 158–163, 1986.
Scher AM. Cardiovascular control. In: *Textbook of Physiology: Circulation, Respiration, Body Fluids, Metabolism, and Endocrinology*, edited by Patton HD, Fuchs AF, Hille B, Scher AM, and Steiner R. Philadelphia, PA: Saunders Company, 1989, p. 972–990.
Scher AM, O'Leary DS, and Sheriff DD. Arterial baroreceptor regulation of peripheral resistance and of cardiac performance. In: *Baroreceptor Reflexes: Integrative Functions and Clinical Aspects*, edited by Persson PB and Kirchheim HR. Berlin: Springer-Verlag, 1991, p. 75–125.
Schobesberger H, Gutkin BS, and Horn JP. A minimal model for metabotropic modulation of fast synaptic transmission and firing properties in bullfrog sympathetic B neurons. *Neurocomputing* 26-27: 255–262, 1999.
Schobesberger H, Wheeler DW, and Horn JP. A model for pleiotropic muscarinic potentiation of fast synaptic transmission. *J Neurophysiol* 83: 1912–1923, 2000.
Shen WX and Horn JP. A presynaptic mechanism accounts for the differential block of nicotinic synapses on sympathetic B and C neurons by *d*-Tubocurarine. *J Neurosci* 15: 5025–5035, 1995.
Simmons MA. The complexity and diversity of synaptic transmission in the prevertebral sympathetic ganglia. *Prog Neurobiol* 24: 43–93, 1985.
Skok VI and Ivanov AY. What is the ongoing activity of sympathetic neurons? *J Auton Nerv Syst* 7: 263–270, 1983.

Smith PA. Amphibian sympathetic ganglia: an owner's and operator's manual. *Prog Neurobiol* 43: 439–510, 1994.

Smith PA and Weight FF. The pathway for the slow inhibitory postsynaptic potential in bullfrog sympathetic ganglia. *J Neurophysiol* 56: 823–834, 1986.

Sun M-K. Central neural organization and control of sympathetic nervous system in mammals. *Prog Neurobiol* 47: 157–233, 1995.

Tosaka T, Chichibu S, and Libet B. Intracellular analysis of slow inhibitors and excitatory postsynaptic potentials in sympathetic ganglia of the frog. *J Neurophysiol* 31: 396–409, 1968.

Tsuji S and Kuba K. Muscarinic regulation of two ionic currents in the bullfrog sympathetic neurone. *Pfluegers* 411: 361–370, 1988.

Usrey WM, Reppas JB, and Reid RC. Specificity and strength of retinogeniculate connections. *J Neurophysiol* 82: 3527–3540, 1999.

Weight FF and Padjen A. Acetylcholine and slow synaptic inhibition in frog sympathetic ganglion cells. *Brain Res* 55: 225–228, 1973.

Yamada WM, Koch C, and Adams PR. Multiple channels and calcium dynamics—modeling bullfrog sympathetic ganglion cells. In: *Methods in Neuronal Modeling from Synapses to Networks*, edited by Koch C and Segev I. Cambridge, MA: MIT Press, 1989, p. 97–133.